Journal of Alloys and Compounds 509 (2011) 8189–8198

Contents lists available at ScienceDirect

Journal of Alloys and Compounds

journal homepage: www.elsevier.com/locate/jallcom

Cationic doping of MgO surfaces to build corrosion protection in Mg alloys

Hyunwook Kwak, Santanu Chaudhuri*

ISP/Applied Sciences Laboratory, Washington State University, Spokane, WA 99210-1495, USA

ARTICLE INFO

Article history:
Received 21 March 2011
Received in revised form 22 April 2011
Accepted 22 April 2011
Available online 30 April 2011

Keywords:
Oxide materials
Point defects
Corrosion
Computer simulations

ABSTRACT

Reactivity of MgO surfaces towards dissociative adsorption of water is crucial in determining the protective performance of oxide films formed on top of Mg alloy surfaces. Engineers and scientists have repeatedly reported that heavy metal contamination could significantly affect the oxide film stability towards water. We performed first-principles analysis on MgO surfaces adsorbed with water molecules in the presence of six different types of cationic impurities – Zn^{2+}, Al^{3+}, Y^{3+}, Mn^{4+}, Zr^{4+}, and Ce^{4+} – to assess the effect of commonly present metal impurities in MgO films on the dissociative adsorption of water. The trend in the adsorption energies with different metal impurities shows that water is less likely to dissociate when cationic impurities with high oxidation states such as Mn^{4+}, Zr^{4+}, and Ce^{4+} are present. Charge transfer from the adsorbed species to the impurity atom is identified as the source of the trend. Increased dissociation barrier for water adsorbed on the same doped surfaces indicates that the incorporation of such impurities will effectively block the dissolution of oxide films and potentially enhance the film's resistivity to water.

1. Introduction

Properties of MgO surfaces are important for its potential use in heterogeneous catalysis [1–4], protective coatings [5–7], and fuel cell applications [8,9]. While the simple rock salt structure makes MgO surface a good representative system for studies of oxide surfaces, its chemical interaction with reactive molecules and ions is not trivial. MgO is inert towards many atoms and molecules. However, excess charge transferred from defect sites of the highly ionic crystal can alter chemical reactivity to other systems such as supported metal clusters [10,11]. In particular, MgO is known to show high reactivity towards water molecules. MgO sample exposed to water undergoes surface hydroxylation that leads to eventual dissolution from surface [12,13]. As a result, the dissolution mechanism at MgO surfaces with water under different thermodynamic conditions has been of particular interest where the initial stage of the dissolution is closely related to the dissociative adsorption of water [12,14–16].

Dissociative adsorption behavior of water on MgO surfaces has been extensively studied both from experiment [16–22] and theory [12–15,23–33]. In the late nineties, hydroxylation of MgO surfaces with different structural geometries and defects were reported in detail by Ferry [17] and Liu [18] using experimental techniques such as low energy electron diffraction (LEED) and Synchrotron X-ray, respectively. Later in the early 2000s, Yu et al. [19] and Kim et al. [20] reported the evidence for partial water dissociation on clean MgO (1 0 0) surface with water coverage close to a monolayer, using techniques such as high resolution electron energy loss spectroscopy (HREELS) and metastable impact electron spectroscopy (MIES), respectively. More recently, a scanning tunneling microscopy (STM) study by Shin et al. [21] has led to an observation of a single water molecule dissociation on MgO (1 0 0) surface by selectively injecting tunneling electrons to the surface.

Since the first report of theoretical evidence for dissociation of water monolayer by Giordano et al. [23], theoretical studies from density functional theory (DFT) [12–14,24–26,33,34], Hartree-Fock (HF) [27,28], and semi-empirical potential calculations [15,29–31] generally agree that the spontaneous dissociation of water molecules is unlikely with an isolated water molecule while it is more likely with the water coverage of monolayer or higher. However, the exact mechanism of the dissociation with monolayer to multilayer of water is yet to be determined.

One of the most significant factors to the dissociative adsorption of water on MgO surface and dissolution of MgO is defect population and the corresponding geometrical aspect. It is well established that the dissociation occurs actively on surface defects such as vacancy, steps, and corners. Theoretically water adsorption and dissociation behavior has been extensively investigated with atomistic-scale modeling of hydroxylated MgO surfaces [12,14,25–27,29,32,35]. In particular, a comprehensive analysis on the water adsorption on various defect sites by Chizallet et al. [32] showed that one can describe the Lewis acidity and basicity of the hydrated surface using thermodynamic modeling, while a combined experimental and theoretical work by Mejias [14] on the

* Corresponding author. Tel.: +1 509 358 7782.
E-mail address: chaudhuri@wsu.edu (S. Chaudhuri).

0925-8388/$ – see front matter © 2011 Elsevier B.V. All rights reserved.
doi:10.1016/j.jallcom.2011.04.125

defected MgO surface dissolution indicates that the dissolution process on MgO surface is also strongly influenced by kinetics of water dissociation on defect sites.

Efforts to understand the adsorption behavior of water on defect populated MgO surfaces is important regarding the protection of Mg alloys from corrosion under humid conditions. While its light weight and high strength–weight ratio gives Mg alloy a great potential in automotive and aviation technology [36], its poor corrosion resistivity by naturally formed oxide films has been one of the biggest obstacles that keep the materials being used for applications that operates in the outdoor environment with high humidity and frequent salt water exposure [36–38].

Corrosion engineers and scientists have repeatedly reported that the presence of more cathodic metals and rare earth (RE) element contamination could result in better corrosion resistance for Mg-based materials. To start with, it is well-known that widely used commercial Mg alloys such as AZ91 series, which mainly consists of Al, Zn, and Mn, show much better corrosion resistance than pure magnesium [36,37]. Introducing Y, Ce, and other rare earth materials to Mg alloy has also been shown effective to enhance corrosion resistance. Direct applications of Y and other RE to Mg alloy such as die-cast Mg–Y–RE–Zn alloy [39,40] (known as WE series), Y/RE enriched alloys with up to 0.8 wt% of Y-rich misch metal [41], Mg–3Nd–0.2Zn–0.4Zr alloy (NZ30K) [42], die-cast Mg–Y binary alloys with up to 6.7 wt% of Y content [43], Mg–Y alloys sputtered [44] or melt-spun [45,46] with 7–26 at.% of Y content, die-cast Mg alloy with up to 3.8 wt% of Ce content [47], and Ce-enriched AE91 [48] and AZ91 [49] with 1–1.7 wt% of Ce content have all shown noticeable enhancement in their corrosion resistance. Pretreatment of AZ31 (Mg–3Zr–Zn) with cerium nitrate solution [50] and conversion coating with Ce and Zr on Mg alloys surfaces [51] were also found showing better corrosion resistance by the protective film conversion.

Similar to pure aluminum and Al alloys, oxide film plays an important role on the corrosion protection of pure magnesium and Mg alloys. Oxide film formed on top of magnesium surfaces has slightly lower corrosion resistance than that of Al surfaces while corrosion resistance of oxide-covered magnesium is often better than that of mild steel [37]. Therefore, protection of the oxide film formed on top of magnesium surface is crucial to the corrosion resistance of the material. For Mg alloys, presence of other alloying compounds than Mg is also important because the alloying species can be transported to the metal surface and affect the composition of the oxide film during the course of corrosion. For example, previous work reported traces of excessive alloying compounds detected at the protective films on top of Y-enriched [43] and Ce-enriched [48–51] Mg alloy systems. In all these cases, the composition change in the protective film by the "doping" of alloyed species is believed to be the key source of their enhanced corrosion resistance. Therefore, understanding the effect of cationic doping towards the protective film stability is crucial to the corrosion protection of Mg alloy. In particular, understanding the doping effect on the water-triggered degradation of oxide films is of significant importance, since MgO film at room temperature is most vulnerable to water-initiated degradation. However, a comprehensive study that discloses the role of cationic impurities on the dissociative adsorption of water on MgO surfaces and the resulting MgO dissolution is still missing.

In this work, we examine the water adsorption behavior on undoped and cation-doped MgO surfaces to assess the potential implications of cationic doping on the integrity of oxide films formed on Mg alloys. Water adsorption energy and the adsorption geometry are examined with slab surface models that have (1 0 0) plane surface and diatomic steps. For the doped surfaces, we introduce six types of impurity elements (Al, Mn, Zn, Zr, Ce, and Y) to our slab surface models. Al, Mn, Zn, and Zr are common ingredients found in many commercial Mg alloys (*e.g.* AZ31, AZ91, AZ91D, etc.), and Y and Ce have been of particular interest as additives in Mg alloys for their role on the enhanced corrosion resistance of the modified protective films [44–51]. Dissociation barriers for water molecules on plane and stepped surfaces are also calculated using nudged elastic band (NEB) method to discuss the kinetic aspect of the doping effect. We investigate the origin of the doping effect by performing Bader charge analysis and discuss the implication of the doping effect regarding the enhanced corrosion resistance of the oxide films.

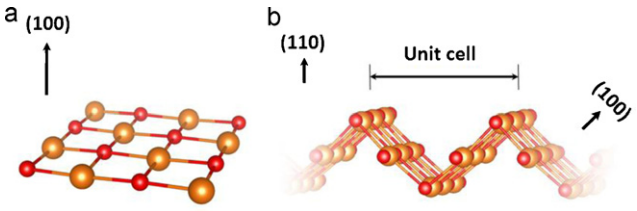

Fig. 1. Illustration of slab surface models for (a) (1 0 0) plane surface and (b) surface with diatomic steps. The plane surface is shown with the size of $(2\sqrt{2} \times 2\sqrt{2})$ primitive unit cell and the surface with diatomic steps is shown with two repeating units of a periodic model. Only surface layer atoms are depicted for clarity.

2. Methods and calculation details

All calculations were performed using spin-polarized density functional theory (DFT) as implemented in VASP [52] with a projected augmented wave technique [53]. Perdew–Burke–Ernzerhof (PBE) functional [54] was applied with plane waves expanded up to 400 eV. All surface models were fully relaxed until Hellmann–Feynman force of every atom is converged within 0.01 eV/Å. The integrations in the Brillouin zone for geometrical optimizations and total energy calculations were performed on Monkhorst–Pack grids of $(2 \times 2 \times 1)$ and $(2 \times 1 \times 1)$ for (1 0 0) plane surface and stepped surface, respectively. For nudged elastic band calculations, only the Γ-point was sampled. 3-D visualization software VESTA [55] was used to visualize the surface adsorption geometries and to analyze them.

We used slab surface geometry to model the MgO surfaces. The initial geometry for the slab surface was based on the rock salt crystal of MgO. The calculated lattice parameter for bulk MgO was 4.242 Å which is in a close agreement with previous predictions from experiment (4.207 Å) [56] and from first principles (*e.g.* 4.261 Å by Haas et al. [57]). Slab surface models with (1 0 0) plane surface and diatomic steps were constructed based on the rock slat structure of bulk MgO. (1 0 0) plane surface model was built from 6 atomic layers of $(2\sqrt{2} \times 2\sqrt{2})$ surface unit cell (16 atoms exposed to vacuum per unit cell surface). Stepped surface model was built from 8 atomic layers of (2×3) surface unit cell of (1 1 0)-oriented slab surface (6 atoms per step edge). To remove monatomic steps at the surface and to create a diatomic step, atoms at every other column of the top-most layer atoms were removed. For both types of slab surfaces, water molecules were introduced only on one side of the slab surfaces. Geometries of the model surfaces are illustrated in Fig. 1.

All slab surface models were subject to 3D periodic boundary condition. Periodic images of a surface were expanded through *xy*-plane while vacuum space of 45 Å was applied in *z*-direction to prevent any interactions between periodic images. With the given slab thickness and the vacuum space, we obtained surface energy of an undoped pristine (1 0 0) surface of 0.872 J/m^2, which only differs from a previously calculated surface energy with GGA + U (0.91 J/m^2) [58] by less than 5%. We also confirmed that the calculated surface energy was converged within 2 mJ/m^2. We applied the dipole correction in *z*-direction for all slab surfaces that has OH-group. Throughout the calculations, we confirmed that the effect of the dipole correction to the adsorption energy of water was less than 0.02 eV (~2 kJ/mol).

Effect of metal doping on MgO surfaces has been widely studied with transition metal species for their promising catalytic performance [59], and the extensive theoretical studies often led to the discovery of key trends in their physical and chemical properties. For example, Yudanov et al. [60] performed systematic DFT calculations on nine different metal atoms (Cr, Mo, W; Ni, Pd, Pt; Cu, Ag, Au) from the periodic table and categorized them into two groups depending on their strength of interaction with surface. Markovits et al. [61] also examined the first-row transition metals to identify a trend in their adsorption properties. More recently, Wang et al. [62] analyzed the trend in the adsorption energy and the charge redistribution on five different types of transition metals (Ni, Pd, Pt, Cu, and Zn). Since the main focus of these works has been on the catalytic performance and surface diffusion properties of the doped species, majority of the atomistic-scale modeling of the doped MgO surface considered metal atoms and clusters adsorbed on top of the surface to represent the deposition of catalytic substances.

On the other hand, detection of the alloying species in the protective layers on top of Mg alloys [43,48–51] suggest that the incorporation of the doping elements

during the corrosion process originates from the transport of these elements from subsurface boundaries and the doped species are likely present in the form of oxide that contains ionized substances. This suggests that the subsurface introduction of metallic substances could become more important than the deposition of metal atoms on top. To reflect this subsurface doping condition more properly, we introduced an impurity site as a substitutional defect replacing one magnesium atom from one of the subsurface lattice sites.

From our slab surface model, doping is done by replacing one Mg at the second layer from the surface with an impurity atom. The second layer from the surface was chosen in particular so that we exclude the case where the defect site is directly exposed to a vacuum and become a potential adsorption site, which could further complicate the charge state of a defect. Impurity sites were embedded with the elements' formal charge states from their most frequent oxide forms (Al^{3+}, Mn^{4+}, Zn^{2+}, Zr^{4+}, Ce^{4+}, and Y^{3+}). To prevent the effect of having unpaired electrons near the surface, all impurity elements except for the isovalent Zn^{2+} are incorporated with the net charge that reflects the formal charge of the impurities from their oxidation states. For these charged impurity sites, homogeneous background charge was applied to keep the net charge in a periodic cell neutral.

3. Results and discussion

3.1. Water adsorption on undoped and impurity-doped MgO (1 0 0) plain surfaces

We calculated the adsorption energy of a water molecule on top of pristine (1 0 0) MgO surface. In this work, structural optimization of an adsorbed water molecule on top of (1 0 0) surface was started from the lowest-energy adsorption geometry reported by Giordano et al. [23] and Cho et al. [33]. In this binding geometry, the O-atom from water is bound to Mg-atom and one of the H atoms is closer to the neighboring surface O. To confirm that the examined adsorption geometry was the lowest energy state, we also examined another water adsorption geometry reported by Finocchi and Goniakowski [12] in which both of the hydrogen atoms from the water molecule are closer to the surface or in other words, pointing inwards to the surface. This configuration is 4 kJ/mol higher in energy than the original adsorption geometry. Therefore, the reported structure is indeed the lowest energy state for the adsorption of an isolated water molecule calculated at the GGA-DFT level using PAW-PBE potentials. The slab surface has 8 adsorption sites (with 8 surface Mg atoms) per periodic unit cell and therefore adsorption of a single water molecule corresponds to 1/8 ML of water coverage. The calculated adsorption energy was $E_{ads} = -36$ kJ/mol. Adsorption energy being negative indicates that the adsorption is an exothermic process. This is in a close agreement with previously calculated adsorption energies of an isolated water molecule ($E_{ads} = -36$ kJ/mol by Odelius [34] and $E_{ads} = -37$ kJ/mol by Cho et al. [33]). Geometry of the adsorbed water on (1 0 0) surface is shown in Fig. 2. The geometry indicates that the adsorption is molecular. The water molecule is slightly tilted. When adsorbed, one of the molecule's OH bonds is extended from 0.97 Å to 1.01 Å. We also found that the surface Mg–O bond closest to the water molecule is increased by 0.1 Å, resulting in a slightly buckled geometry at the surface. A dissociative adsorption geometry where OH and H groups are adsorbed each on neighboring surface Mg and O sites was also examined for comparison, yet no stable dissociative adsorption geometry was found at this stage. This is consistent with the previous report by Odelius [34] where it was reported that the dissociative adsorption is not favored at the surface with such a low coverage.

We also examined the coverage dependence of the water adsorption energy by calculating the adsorption energy with larger than 1/8 ML of coverage. We increased the number of adsorbed molecule to 2, 4, 6, and 8, which correspond to the surface coverage of 1/4, 1/2, 3/4, and 1 ML, respectively. The adsorption energies calculated with different coverage are summarized in Table 1. The results show that the molecular adsorption of water becomes more stable as the coverage increases. The adsorption energy with coverage of 1/2 ML is somewhat lower than the value Ahdjoudj et al.

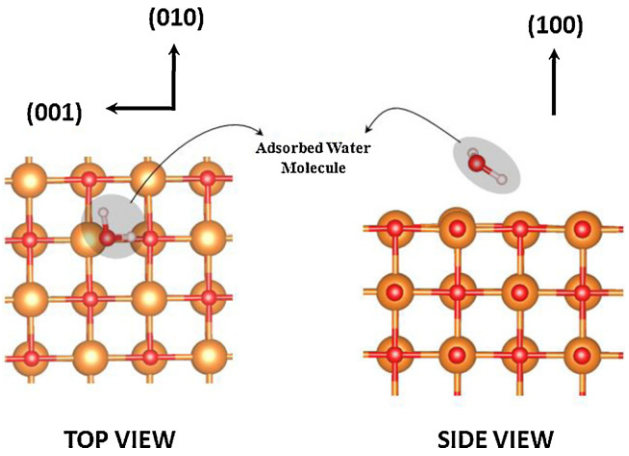

Fig. 2. Relaxed surface geometry of an isolated water molecule adsorbed on pristine (1 0 0) surface. Water molecule and the top-three layers of surface Mg and O atoms are shown. Large-, medium-, and small-sized spheres represent Mg, O, and H atoms, respectively.

Table 1
Water adsorption energy on (1 0 0) MgO surface with respect to coverage.

Coverage (ML)	E_{ads} (kJ/mol)
1/8	−36
1/4	−45
1/2	−46
3/4	−57
1	−53

[28] obtained from Hartree-Fock calculations (70.7 kJ/mol) but the adsorption energy with coverage larger than 1/2 ML is in a good agreement with the previously calculated adsorption energy by Simpson [15] where the adsorption energy was predicted to be close to 60 kJ/mol with coverage close to 1 ML. Also from our calculations, the adsorption energy reaches its maximum at 3/4 ML and starts decreasing. This is likely owing to the repulsive interaction between the adsorbed molecules triggered by the dense population of water at the surface. We also identified a partial dissociative adsorption state with 1/4 ML coverage, where one of the two adjacent water molecules adsorbed is dissociated. The calculated adsorption energy of the corresponding geometry is $E_{ads} = -57$ kJ/mol. This is more stable than molecular water adsorption ($E_{ads} = -45$ kJ/mol) with the same 1/4 ML coverage. However, we cannot provide the relative stability of the surface with all the water molecules dissociated as they tend to re-associate back during geometry optimization.

We calculated the water adsorption energy in the same manner for (1 0 0) surface with cationic impurities. Water coverage was fixed as 1/8 ML and the impurity was placed right beneath the surface oxygen atom closest to the water molecule. The calculated adsorption energies on the doped (1 0 0) surfaces are listed in Table 2. The results show that the adsorption of a water molecule is further stabilized by the cationic impurities. There is also a strong trend in the water adsorption energy with respect to the impurity

Table 2
Water adsorption energy on impurity doped (1 0 0) MgO surfaces.

Impurity	E_{ads} (kJ/mol)
Zn^{2+}	−36
Al^{3+}	−74
Y^{3+}	−84
Mn^{4+}	−120
Zr^{4+}	−146
Ce^{4+}	−155

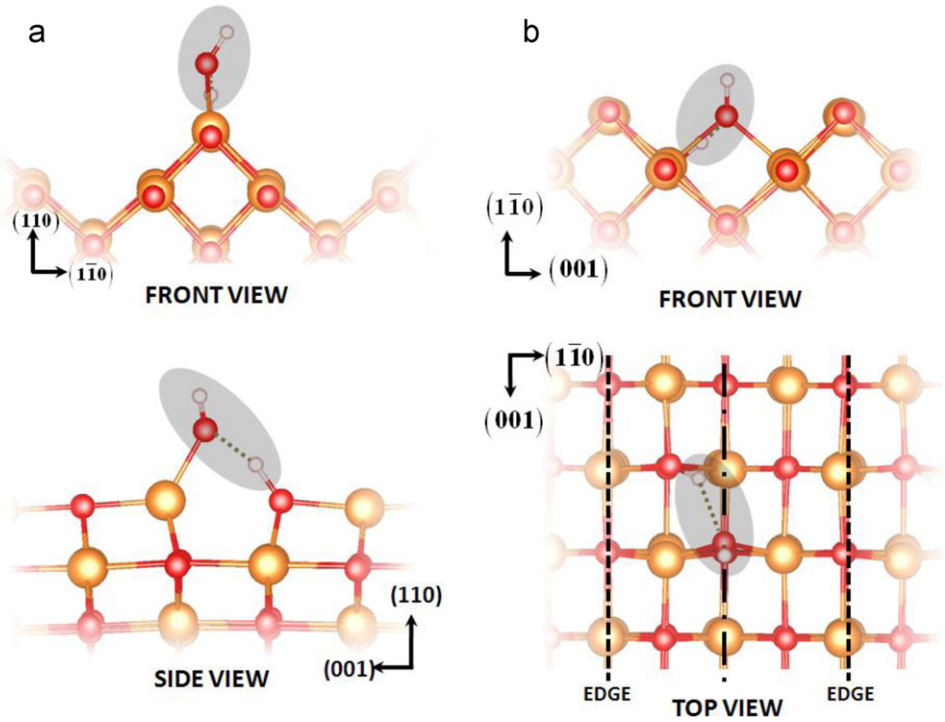

Fig. 3. Surface geometry of an isolated water molecule adsorbed (a) on the edge and (b) in the valley of a diatomic step on MgO surface. Water molecule and surface atoms from the top-three layers are shown. Large-, medium-, and small-sized spheres represent Mg, O, and H atoms, respectively. Dotted lines indicate the semi-dissociated OH bonds at 1.46 Å in viewgraph (a), dissociated O–H distance of 1.87 Å in (b), respectively. The dissociation considerations are with respect to other covalent OH bonds from Mg–OH domains which are much shorter (0.97 Å).

doping—the adsorption energy increases by almost 2–4 times when the surface is doped with impurities with oxidation state higher than 2+.

We also notice the change in the adsorption geometry with doping. Fig. 4(a)–(c) summarizes the change in the adsorption geometry on (1 0 0) plane surfaces triggered by the doped impurities. We found that on Al^{3+}-, Y^{3+}-, Mn^{4+}-, Zr^{4+}-, and Ce^{4+}-doped surfaces, water molecule sits on top of the surface Mg atom and is not tilted like a water molecule adsorbed on undoped or Zn^{2+}-doped surfaces. On these surfaces, O–H bond lengths of water are not significantly different before and after the adsorption as well. The surface Mg–O bond length at the adsorption site on these surfaces was a bit larger (increased by up to 5%) than on undoped or Zn^{2+}-doped surfaces, leading to a slightly more buckled surface.

3.2. Water adsorption on undoped and doped MgO surfaces with diatomic steps

Defect sites are known to be active source of hydration of MgO surface, and step site in particular is important for its frequent occurrence on (1 0 0) surface with relatively lower formation energy than the defect complexes [14,32]. To take the step site hydration into account, we also calculated the water adsorption energy on the surface with diatomic steps using the (1 1 0)-oriented slab surface model. Each edge of a step has six surface atoms (three Mg and three O) per periodic surface unit cell. We examined the adsorption of an isolated water molecule both on the edge and in the valley of the diatomic step. For the starting configurations on the stepped surfaces, the water molecule was placed on top of one of the surface edge Mg sites, resulting similar geometry as shown in Fig. 4(f). The initial distance between the surface Mg and the water O was set as 2.1 Å. We could not locate any other minima for water for the stepped surface other than the one reported. Calculated adsorption energies for edge-adsorbed and valley-adsorbed water molecules were −126 kJ/mol and −89 kJ/mol, respectively. While we see that water adsorption is more favored on the edge than on the valley, the adsorption both on the edge and in the valley are much stronger than on (1 0 0) plane. This agrees well with other previous reports on MgO surfaces with water adsorption [13,26,29,32,35] where non-ideal surfaces and surfaces with steps show stronger interaction with water. The stronger adsorption on the edge site than on (1 0 0) plane can be understood by the less-coordinated atoms at the surface further stabilizing the chemisorptions of water molecule. The stronger adsorption on the valley site than on (1 0 0) plane can be understood by the increased interactions with more surface atoms.

Unlike water molecules adsorbed on (1 0 0) surfaces, we also found that the water molecules on step sites are semi-dissociated with one of its OH bonds extended with a bond length up to 1.45 Å (bond length increased by 51%). The resulting adsorption geometries are illustrated in Fig. 3. Since the dissociation of water molecules is the key to the dissolution mechanism on the oxide surfaces [14], the semi-dissociated water molecule suggests that the steps on oxide surfaces should provide more active sites for dissolution of surface atoms than on plane surfaces. We also found that the Mg–O bond length at the adsorption site on the edge is extended up to 2.75 Å (increased by 30%). The extended Mg–O bond length at the adsorption site is larger than the bond length at the adsorption site on (1 0 0) surface.

We introduced the same six types of cationic impurities we examined with (1 0 0) surface to diatomic step sites to examine the effect of both doping and defect presence on the adsorption behavior. An impurity atom was used as substitutional dopant to replace the atom beneath the surface Mg atom of the adsorption site.

Table 3 lists the adsorption energies of water molecules adsorbed on the doped surfaces. Changes in the adsorption geometry triggered by the doping are also summarized in Fig. 4(d)–(f). The change in the adsorption energy by doping is smaller than the change from (1 0 0) surfaces, but the same trend holds for the adsorption energy with respect to the oxidation state of an impu-

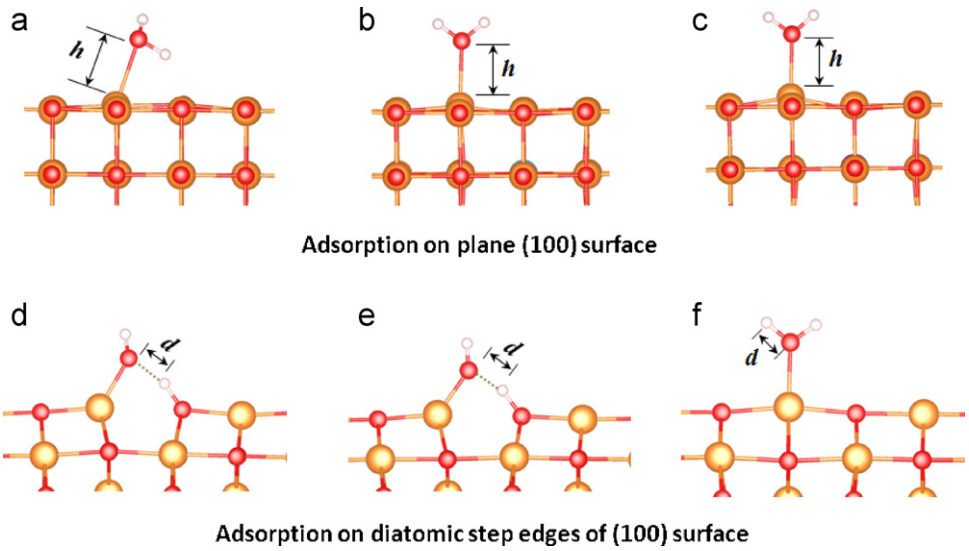

Fig. 4. Water adsorption geometry of an isolated water molecule adsorbed on doped surfaces. The top three illustrates the adsorption geometry on (1 0 0) plane doped with (a) Zn^{2+} (h = 2.31 Å), (b) Al^{3+} (h = 2.19 Å), Y^{3+} (h = 2.15 Å), and (c) Mn^{4+} (h = 2.16 Å), Zr^{4+} (h = 2.12 Å), Ce^{4+} (h = 2.11 Å). The bottom three illustrates the adsorption geometry on diatomic step edges doped with (d) Zn^{2+} (d = 1.47 Å), (e) Al^{3+} (d = 1.32 Å), Y^{3+} (d = 1.32 Å), and (f) Mn^{4+} (d = 0.98 Å), Zr^{4+} (d = 0.98 Å), Ce^{4+} (d = 0.98 Å). Large-, medium-, and small-sized spheres represent Mg, O, and H atoms, respectively. Dotted lines indicate the semi-dissociated OH bonds. All other OH bonds have much shorter bond length (0.97 Å).

rity element—adsorption is stronger when an impurity with higher oxidation state is present.

Fig. 4 shows that the change in the adsorption geometry triggered by doping is more significant on step edges than on (1 0 0) plane. The adsorption geometry for Zn^{2+}-doped surface shows negligible difference when compared with undoped surface, while dissociation of a water molecule on Al^{3+}-, Y^{3+}-doped surfaces becomes slightly less effective than on an undoped surface with a shorter OH bond length (1.32 Å, bond length increased by 38%). For Mn^{4+}-, Zr^{4+}-, and Ce^{4+}-doped surfaces, the adsorbed water molecule does not reveal any evidence of a semi-dissociated adsorption geometry and is virtually identical to the ones from the same-element-doped (1 0 0) surfaces.

3.3. Doping effect on the dissociative adsorption of water

Aside from the apparent trend in the water adsorption energy, the varying adsorption geometry of a water molecule at a step edge of MgO surfaces with different cationic doping also has an implication on the dissociative adsorption of water. First, larger water adsorption energy on (1 0 0) plane sites with 3+ and 4+ impurities indicate that the dissociation of water by O–H bond breakage could require more energy on the doped surfaces because the water molecule is more tightly bound to the surface atom. It is also noticeable from the stepped surfaces doped with Mn^{4+}, $Zr^{4+}$and Ce^{4+} impurities that the water molecule does not show any hint of semi-dissociation as on the step edges of undoped surface. It indicates that the step edge sites with such doped surfaces may not be as kinetically active to the water dissociation as on the undoped surfaces because of the stronger OH bond of water.

Table 3
Water adsorption energy on diatomic step edges of impurity doped MgO surfaces.

Impurity	E_{ads} (kJ/mol)
Zn^{2+}	−126
Al^{3+}	−128
Y^{3+}	−122
Mn^{4+}	−137
Zr^{4+}	−171
Ce^{4+}	−174

To investigate this idea further, we calculated the energy barriers for dissociation of an adsorbed water molecule both on (1 0 0) and stepped surfaces. The same six impurities we examined for the doping effect on the adsorption energy was also introduced. Nudged elastic band method with climbing image algorithm (CI-NEB) [63] was used to calculate the dissociation barrier of a water molecule on top of these surfaces. To set up the transition state calculation, we used the optimized geometry of water adsorbed surface as the initial (adsorbed) state. The final geometry for the dissociated water on both (1 0 0) plane and stepped surfaces were prepared based on the recent study of a single water adsorption on MgO (1 0 0) surface by Shin et al. [21] where dissociated OH group sits on top of the bridging site between the two neighboring surface Mg atoms. Fig. 5 illustrates the geometries of the dissociated state on surfaces with (1 0 0) plane and diatomic steps. The total of five images between the initial and the final geometries were employed to find the minimum energy paths for the dissociation. With climbing image algorithm, one of the images with the highest energy climbs up to the saddle point during the NEB calculation so that the correct value for the energy barrier can be obtained.

Table 4 summarizes the calculated dissociation enthalpies and the dissociation barriers on the doped surfaces. The results show that the dissociation barrier is higher both on the (1 0 0) plane and on the step edges when the surface is doped with Al^{3+} or Zr^{4+}. This indicates that the surface dissociation of water can be effectively inhibited by the presence of these impurities. In addition, we note that our calculation shows the trend in the dissociation enthalpy does not as clearly reflect the trend in the dissociation barrier on the step edges. This indicates that the analysis solely based on the thermodynamic information can sometimes be misleading when the actual trend in the dissociation mechanism is dominated by the kinetic factors. Therefore, our work shows that the transition state analysis will be critical to take such kinetic aspect into account.

Since dissociative adsorption of water is a key to the initiation of the oxide dissolution at the surface, the results back up the idea that the presence of cationic impurities with high oxidation states will effectively block the introduction of proton and hydroxide ion through dissociative adsorption of water at defected surface sites. We also found that the doping effect on the water dissociation barrier is less explicit on the step sites than on the (1 0 0)

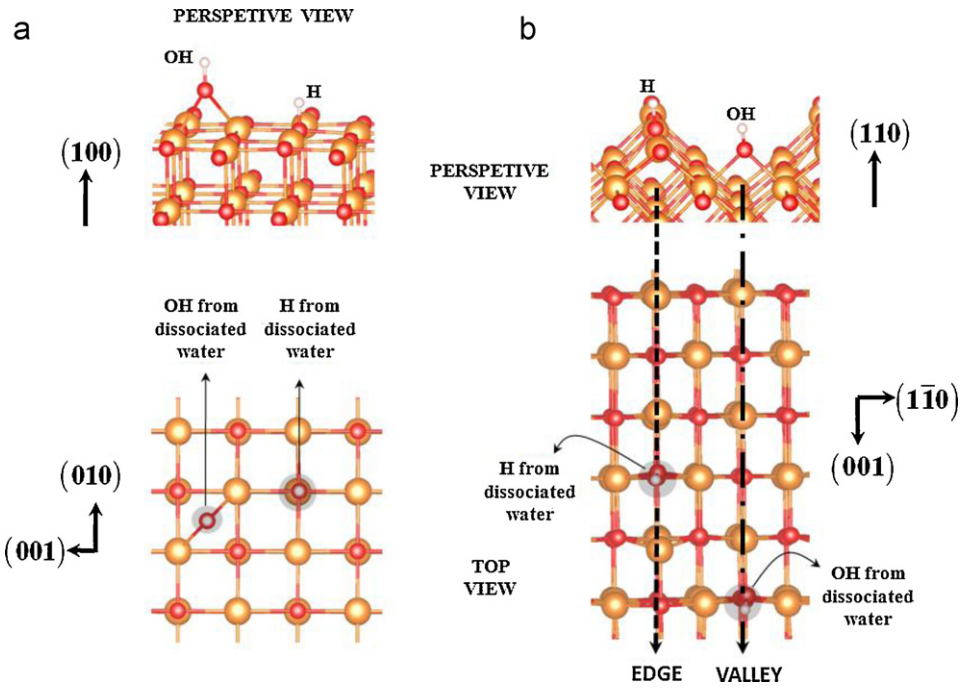

Fig. 5. Geometry of adsorbed proton and hydroxide resulting from water dissociation on (a) (1 0 0) plane and (b) edge of a diatomic step. Mg–O bond lengths for the dissociated OH group are also shown. Large-, medium-, and small-sized spheres represent Mg, O, and H atoms, respectively.

sites. This suggests that the presence of such impurities will block the dissolution process more effectively on the plane surface than on the stepped or defected surfaces in general. In this sense, such cationic impurities could ultimately control the large scale dissolution mechanism by altering the preferential dissociation sites for water at the surface. Therefore, the enhanced corrosion resistance of the oxide films on top of some Mg alloys can partly explained by the presence of these impurities that are in contact with surfaces and grain boundaries of oxide films. To complete the argument, however, more rigorous analysis on the water adsorption behavior for other types of non-ideal surface geometries (*e.g.* point defects, divacancy sites, hydrated polar surfaces, etc.) needs to be followed in the future.

3.4. Bader charge analysis and projected density of states analysis

The trend in the adsorption behavior with respect to the oxidation state of the doped impurity suggests that the effect of impurity doping may have electronic origin. Such electronic effect can only be properly understood if one describes the electronic interactions between atoms and molecules properly. One way to do this is to decompose the electronic structure into contributions from individual atoms, using a particular partitioning scheme.

Bader [64] suggested an elegant scheme for such partitioning—he suggested that one could divide space into atomic (Bader) volumes from a given charge density. Each Bader volume is occupied with partitioned (Bader) charge and is separated from other volumes by surfaces on which the charge density is a minimum normal to the surface and. There is typically one charge density maximum at each atomic center and one Bader volume for each atom, but there are cases in which Bader volumes do not contain an atom site [65]. The Bader partitioning has an advantage over other partitioning schemes such as Mulliken population analysis or wave function-based population methods in such a way that the partitioning is independent of a basis set and is based upon an observable quantity—charge density [66–68].

We used a grid-based Bader partitioning algorithm developed by Tang et al. [68] to partition each atomic volume of a water molecule adsorbed on undoped and impurity-doped surfaces. After the partitioning, charges that are assigned to the adsorbed species were compared with the charge of an isolated water molecule. Any deviation from the charge of an isolated water molecule would indicate the charge transfer triggered by the adsorption. These charge transfer amounts for the adsorbed water on the doped surfaces are listed in Table 5.

On the molecular adsorption on (1 0 0) surfaces, we indicate that the amount of charge transfer is not larger than 0.1*e* for all surfaces. The values are relatively small because molecular adsorption with little change in the structure of an adsorbed species would not result in any significant amount of charge transfer. However,

Table 4
Dissociation barrier (E^*_{dis}) and dissociation enthalpy (ΔE_{dis}) for O–H bond of a surface-adsorbed water molecule on (1 0 0) surface sites and step edges with the presence of different cationic impurities.

Impurity	(1 0 0)		Step edge	
	E^*_{dis} (kJ/mol)	ΔE_{dis} (kJ/mol)	E^*_{dis} (kJ/mol)	ΔE_{dis} (kJ/mol)
None	93	89	143	96
Zn^{2+}	74	69	144	95
Y^{3+}	136	131	143	112
Al^{3+}	135	128	156	100
Mn^{4+}	195	186	169	94
Zr^{4+}	214	205	174	101
Ce^{4+}	170	160	161	106

Table 5
Amount of charge transfer occurred between surface and adsorbed species calculated from the Bader charges. Positive/negative values indicate gain/loss of electrons from the adsorbed species. "Molecular" denotes the molecular adsorption state and "Dissociated" denotes the dissociative adsorption state where single proton and OH are separated upon the adsorption resulting in the adsorption geometry from Fig. 5.

Impurity	(1 0 0) plane		Diatomic step edge	
	Molecular	Dissociated	Molecular	Dissociated
None	+0.07*e*	−0.11*e*	−0.20*e*	−0.11*e*
Zn^{2+}	+0.07*e*	−0.11*e*	−0.20*e*	−0.11*e*
Al^{3+}	−0.02*e*	−0.13*e*	−0.15*e*	−0.11*e*
Y^{3+}	−0.02*e*	−0.13*e*	−0.13*e*	−0.11*e*
Mn^{4+}	−0.04*e*	−0.12*e*	−0.05*e*	−0.13*e*
Zr^{4+}	−0.03*e*	−0.15*e*	−0.03*e*	−0.12*e*
Ce^{4+}	−0.04*e*	−0.15*e*	−0.03*e*	−0.12*e*

there is one thing that is noticeable from undoped and Zn-doped surfaces—their direction of charge transfer is opposite to that of all the other doped surfaces. This can be directly linked to the slightly tilted water adsorption geometry from undoped and Zn-doped surfaces (see Fig. 4(a)). Since these two surfaces are the only surfaces with positive signed charge transfer and the tilted adsorption geometry, the slight change in the adsorption geometry is believed to be the source of the minute difference in their charge transfer behavior.

For the step edge site adsorptions on undoped and Zn^{2+}-, Al^{3+}-, Y^{3+}-doped surfaces, we see the adsorption brings relatively larger amount (>0.1*e*) of electron transfer from molecule to surface. With this, another direct relationship between the charge transfer behavior and the adsorption geometry is identified—all the adsorption state that brings transfer of charge larger than 0.1*e* also show semi-dissociated adsorption geometry (Fig. 4(d) and (e)). This indicates the interaction between surface and water molecule on these surfaces became stronger to give more noticeable changes in the molecular adsorption geometry.

For the step edge site adsorptions with impurities that have oxidation state of 4+ (Mn^{4+}, Zr^{4+}, or Ce^{4+}), we notice little difference in their charge transfer behavior when compared with the plane site adsorption. This is consistent with our earlier observation that both the adsorption geometry and the adsorption energy do not vary significantly from plane site to step edge site adsorptions when surface is doped with Mn^{4+}, Zr^{4+}, or Ce^{4+}.

In addition to the charge analysis on the molecular adsorption states, we performed similar charge analysis on the dissociative adsorption state of water in order to assess the impact of metal doping on the charge transfer behavior during complete dissociation of water. Surface geometries for the dissociative adsorption

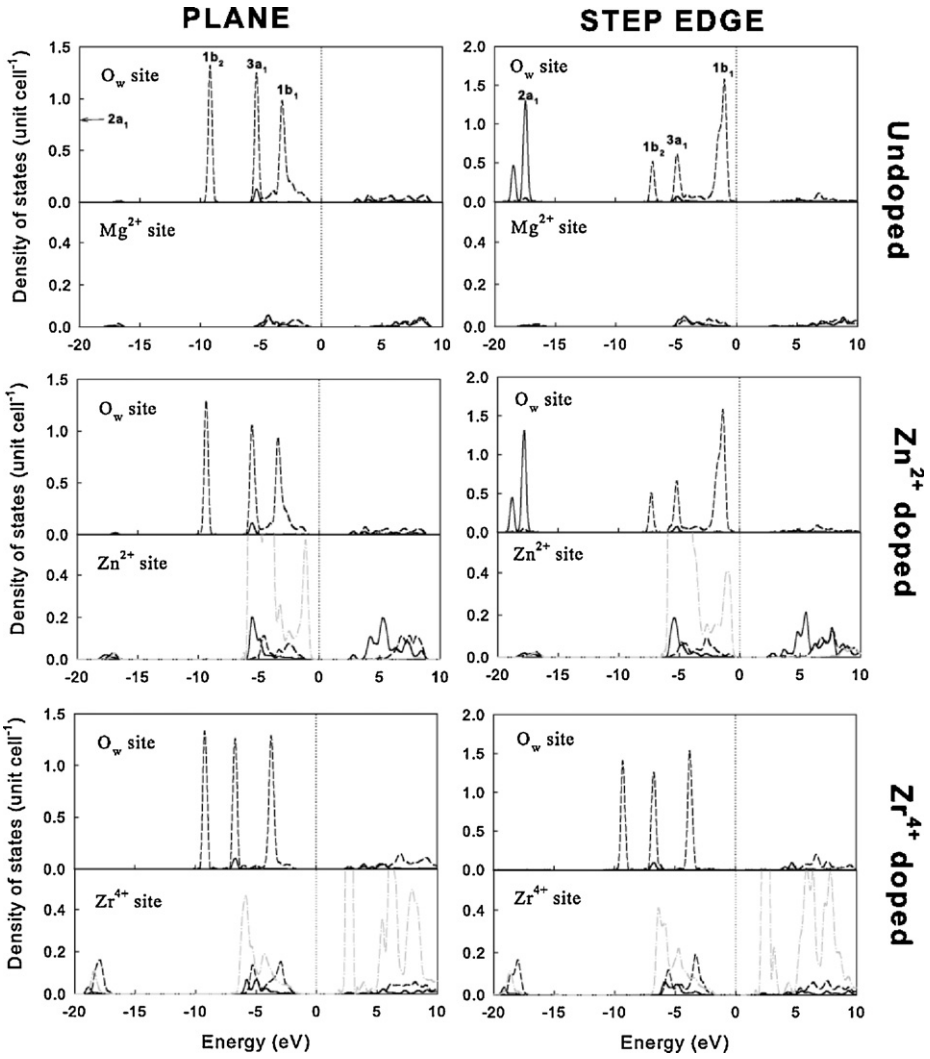

Fig. 6. O_w and impurity site projected densities of states (DOS) from undoped, Zn^{2+}-doped and Zr^{4+}-doped surfaces. Calculated DOS from both plane and step edge sites are shown. Solid and dashed lines depict *s*- and *p*-wave projected DOS, respectively. Dashed-dot lines (colored grey) are from *d*-wave projections. For O_w site projected DOS from undoped surfaces, each of the first four peaks below the Fermi level (dotted line) is labeled with bonding orbital of water.

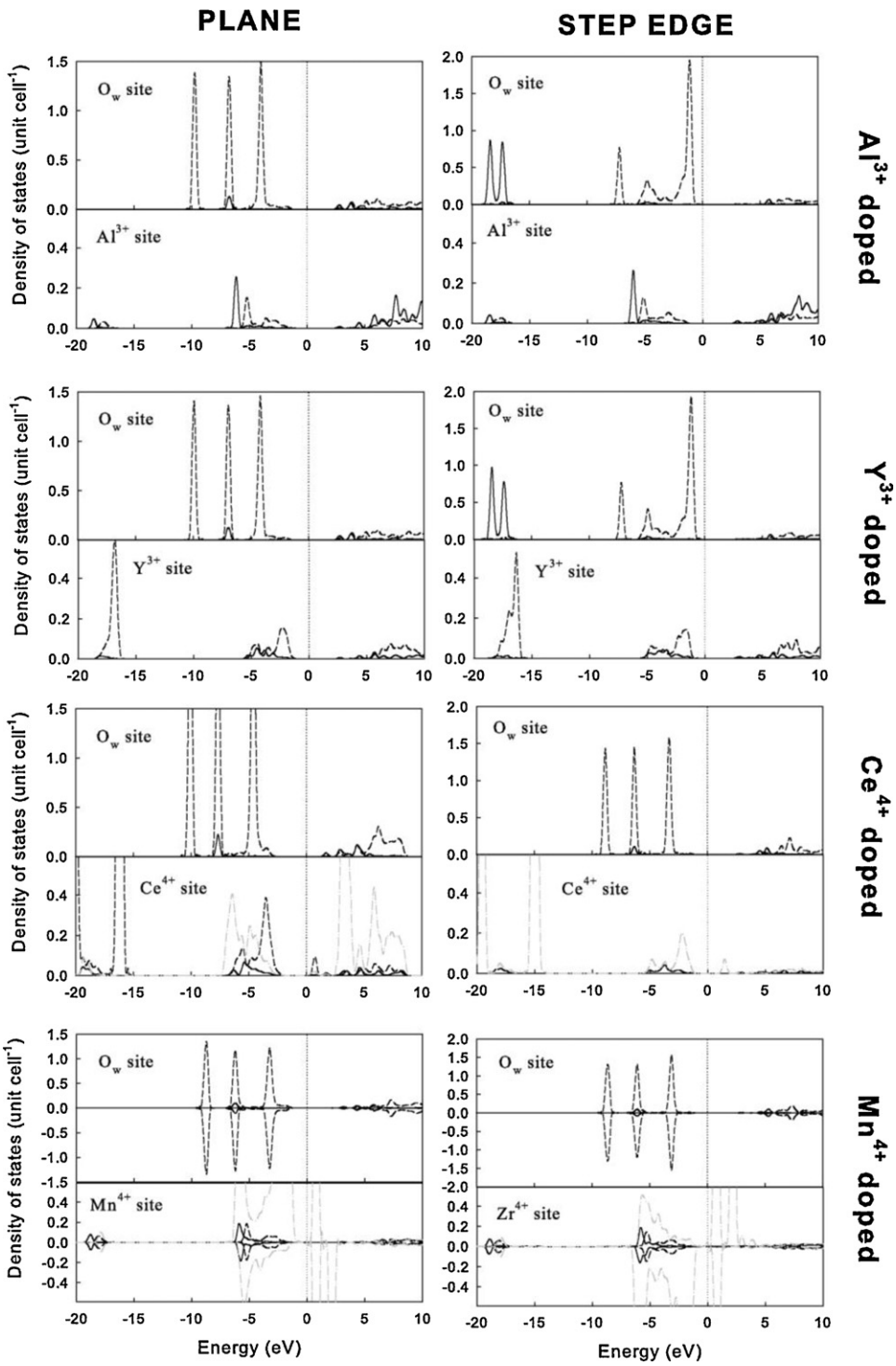

Fig. 7. O_w and impurity site projected densities of states (DOS) from Al^{3+}-doped Y^{3+}-doped, Ce^{4+}-doped, and Mn^{4+}-doped surfaces, plotted in the same manner that Fig. 6 was plotted. For (spin-polarized) Mn^{4+}-doped surfaces, both spin up and down states are depicted.

states were taken from the final-state image of the earlier CI-NEB calculations. Each surface consists of a proton and an OH group individually adsorbed near the original molecular adsorption site (Fig. 5). Bader charge for the adsorbed species after the dissociation was then calculated by adding up the charges of proton and OH sites.

Transferred charge values for the dissociative adsorption states are listed in Table 5 along with the results from the molecular adsorption states. The complete dissociation of water on MgO surfaces costs about 0.11*e*–0.15*e* of electrons per water molecule and the amount of charge transfer do not depend as much on the adsorption site geometry or on the types of impurity element. As a result, the charge transfer behavior during the whole dissociative adsorption process is likely to be affected more by the molecular adsorption states and less by the final dissociated states. For example, charge transfer behavior would be significantly different from plane site adsorption to step edge site adsorption for undoped and Zn^{2+}-doped surfaces, because the amount of charge that are transferred to the molecular adsorption state dramatically changes with respect to the adsorption site geometry (+0.07*e* for plane site

to −0.20*e* for step edge site). Conversely, any dissociating water molecule on Mn^{4+}-, Zr^{4+}-, and Ce^{4+}-doped surfaces would not be affected as much by the adsorption site geometry, because charge transfer values from their molecular adsorption states do not vary significantly.

3.5. Projected density of states analysis

Projected density of states analysis often provides resourceful information when combined with other first-principles-based electronic structure analysis like transition state and charge state analysis. For more detailed understanding of the water adsorption behavior with the impurities we examined, we calculated and plotted angular-projected density of states at the adsorption site and at the impurity site, respectively. The adsorption site DOS were calculated from an atomic volume centered at the oxygen site from water molecule. The impurity site DOS was calculated from an atomic volume centered at the impurity site. For a clearer comparison, we first show the projected DOS from undoped, Zn^{2+}-doped, and Zr^{4+}-doped surfaces in Fig. 6 which represent surfaces with no impurities, impurities with low oxidation state, and impurities with high oxidation state, respectively. Projected DOS from all other surfaces are shown in Fig. 7.

In all O_w site projected DOS, peaks from all four of the bonding orbital of water can be identified. From lower to higher in energy, each of the four peaks can be assigned to $2a_1$, $1b_2$, $3a_1$, and $1b_1$ state of the bonding orbital of water, respectively. Angular dependent projection also confirms that $2a_1$ level comes from the *s*-state and the rest that are closer to the Fermi level come from the *p*-state. If these peaks from O_w site projected DOS are sharp and well separated one another from the surface projected DOS, it would indicate that the electronic structure of the adsorbed water molecule is close to that of an isolated water molecule. If the peaks are noticeably broadened or shifted, it would indicate the altered electronic structure of the adsorbed water by its interaction with surface.

In the figure, it is found from both undoped (1 0 0) plane and step edge sites that the peak that corresponds to $1b_1$ state is noticeably broadened. As a result, there is no clear separation between $3a_1$, and $1b_1$ states. The O_w site projected DOS from Zn^{2+}-doped surfaces do not show any significant difference with those from undoped surfaces, which indicate that the electronic effect of Zn^{2+} on the adsorbed molecule is minimal. On the other hand, all peaks from the O_w site projected DOS from Zr^{4+}-doped surfaces are sharp and well separated. This indicates that the adsorbed water molecule on Zr^{4+}-doped surfaces behaves more like an isolated molecule and less like a strongly chemisorbed species. Therefore, water adsorbed on Zr^{4+}-doped surfaces will be farther from the final stage of any dissociative surface adsorption. We also note that when impurities with intermediate oxidation state such as Al^{3+} and Y^{3+} are doped (Fig. 7), the projected DOS show dependence on surface geometry, *i.e.* projected DOS from plane site shows almost the same feature from that of undoped or Zn^{2+} doped surfaces, while projected DOS from step edge site shows similar feature from 4+ impurity doped surfaces. The trend with the oxidation state of the impurity is consistent with our earlier observations on the water adsorption behavior with these impurities.

While the projected DOS at O_w site agrees well the predicted doping effect on the adsorption behavior, the origin of such behavior can be also identified by comparing it with the impurity site projected DOS. From Figs. 6 and 7, a comparison between each of the O_w site projected and the impurity site projected DOS of the doped surfaces clearly indicate that there is an overlap between the impurity *p*- and *d*-states at the impurity site and the $1b_1$ state. In particular, it is found that the electronic density of the impurity *p*-states at the overlapping region is higher at Mn^{4+}, Zr^{4+}, and Ce^{4+} sites than at Zn^{2+} site. This indicates that the *p*-state electrons that cause the $1b_1$ state broadening at O_w site have been transferred to the impurity site only when an impurity with high oxidation state such as Mn, Zr, and Ce are introduced. Therefore, it leads to the same conclusion from the Bader charge analysis that the charge transfer from surface adsorption states to bulk impurity states causes the doping effect that is oxidation-state dependent.

Both Bader charge analysis and projected DOS analysis point out that the doping effect comes from the changes in the electronic structure, which leads to a charge transfer from adsorbed species to impurity atoms. With this, one can explain why similar adsorption behavior is predicted for the surfaces doped with impurities that have the same oxidation state. Based on this argument, it is also possible to make a series of qualitative predictions for the water adsorption behavior with wide range of different cationic impurities, based on their preferred state of oxidation. For example, one could expect that the presence of impurities that have similar oxidation state as Mn, Zr, and Ce will be as effective in terms of resistance to water-activated degradation, while other isovalent impurities like Zn will show minimal impact. For a definitive conclusion, more rigorous analysis in much larger length scale with other types of defects and impurities is expected in future work.

4. Conclusions

We studied the water adsorption behavior on cation doped MgO (1 0 0) surface with diatomic steps. Six types of impurities (Zn^{2+}, Al^{3+}, Y^{3+}, Mn^{4+}, Zr^{4+}, and Ce^{4+}) were examined with the adsorption energy and the adsorption geometry of a water molecule. On (1 0 0) surface with 1/8 ML coverage, we confirmed that the adsorption is molecular and the dissociation of water is not likely to occur spontaneously. On surfaces with diatomic steps, we found that the adsorption at the edge is most favorable energetically and that the adsorbed water molecule is semi-dissociated with one of its OH bonds extended by up to 51%.

The results from the impurity-doped surfaces show that the doping significantly affects the adsorption energy as well as the adsorption geometry of a water molecule. The trend in the adsorption energies indicates that the doping metals with higher oxidation number lead to a more stable adsorption of water. The trend in the adsorption geometry also suggests that the water molecules adsorbed on the step edges is less likely to dissociate when the surface is doped with such elements. Transition state calculation using CI-NEB for water dissociation confirms the effect of raising the water dissociation barriers by doping except for Zn^{2+}. Based on the Bader charge analysis, we conclude that the trends should originate from the difference in the amount of charge transfer from an adsorbed water molecule to the surface, triggered by the impurity atoms.

The work shows that the presence of the cationic impurities such as Mn^{4+}, Zr^{4+}, and Ce^{4+} in MgO could significantly raise the water dissociation barrier on surfaces, potentially increasing the resistance of the oxide film towards the water-activated degradation. The results also suggest that the presence of such elements in Mg alloy systems will affect the large scale dissolution mechanism of oxide films formed on top of them by altering preferential dissociation sites at the surface, which will significantly affect their corrosion behavior in microscopic length scale.

The doping effect predicted from this work is consistent in particular with the previous experimental observations that the oxide films containing Ce and Zr [45,46,49,51] show much better corrosion resistance. We also note that our subsurface introduction of impurities has led to a significant dependence of the doping effect on the formal charge of the impurities. This suggests that the doping effect on the protective film for alloy surfaces should be different in nature from the doping effect on the metal atoms and clusters deposited on oxide surfaces. This work sets up the

first theoretical ground for such effect if impurity in regards of enhanced corrosion resistance of Mg alloy. In the future, we expect to perform more rigorous analysis on such doping effect in larger length scale for a definite conclusion throughout the whole mechanism of oxide film degradation. Of course, like any alloys, the importance of a protective microstructure of the surface films sometimes outweighs the role of RE in the alloy formulation. There are examples of such alloys that are vulnerable to corrosions even with high RE doping levels. As a result the corrosion protection is dependent of many different aspects of the surface film exposed to humid environment and pH changes. Also, the performance of Mg alloys and the integrity of surface films under the standard scribe tests and exposed to an ASTM-B117 salt-fog environment are often considered the gold standard. The damaged film and rebuilding of protective environment is particularly difficult under the continuous wet environment. It is therefore often the surface pre-treatment that becomes of prime importance to show better ASTM-B117 performance (hence the prevalence of chromated coatings) and some of our current focus is therefore somewhat misplaced due to accelerated testing protocols in defense and industrial applications. A deeper understanding of Mg alloys and their composition specific vulnerabilities will require a concerted effort between modeling and experimental efforts to identify the uniqueness or peculiarities in the failure modes for each alloy systems. This may include a renewed stress on understanding re-growth of the oxide film when damaged for understanding the repair mechanisms, composition of the intermetallic precipitates, and doping grain-boundaries with appropriate RE to improve performance.

Acknowledgements

Research was sponsored in part by the Army Research Laboratory and was accomplished under Cooperative Agreement Number W911NF-10-2-0112. The views and conclusions contained in this document are those of the authors and should not be interpreted as representing the official policies, either expressed or implied, of the Army Research Laboratory or the U.S. Government. The U.S. Government is authorized to reproduce and distribute reprints for Government purposes notwithstanding any copyright notation herein. The rest of the funding is from the Office of Naval Research grant #s N00014-04-1-0688 and N00014-06-1-0315.

References

[1] H.H. Hu, E. Ruckenstein, Catal. Rev. 44 (2002) 423.
[2] Y. Hao, M. Mihaylov, E. Ivanova, K. Hadjiivanov, H. Knozinger, B. Gates, J. Catal. 261 (2009) 137–149.
[3] L. Lefferts, K. Seshan, B. Mojet, J. Vanommen, Catal. Today 100 (2005) 63–69.
[4] S. Wang, Z.H. Zhu, Energy Fuels 18 (2004) 1126–1139.
[5] J. Liang, P.B. Srinivasan, C. Blawert, W. Dietzel, Corros. Sci. 51 (2009) 2483–2492.
[6] T. Lei, C. Ouyang, W. Tang, L. Li, L. Zhou, Corros. Sci. 52 (2010) 3504–3508.
[7] Q. Cai, L. Wang, B. Wei, Q. Liu, Surf. Coat. Technol. 200 (2006) 3727–3733.
[8] S. Adhikari, S.D. Fernando, S.D.F. To, R.M. Bricka, P.H. Steele, A. Haryanto, Energy Fuels 22 (2008) 1220–1226.
[9] F. Marino, Appl. Catal. B: Environ. 54 (2004) 59–66.
[10] V. Henrich, The Surface Science of Metal Oxides, Cambridge University Press, Cambridge, New York, 1994.
[11] B. Yoon, Science 307 (2005) 403–407.
[12] F. Finocchi, J. Goniakowski, Phys. Rev. B 64 (2001) 125426.
[13] K. Refson, R. Wogelius, D. Fraser, M. Payne, M. Lee, V. Milman, Phys. Rev. B 52 (1995) 10823–10826.
[14] J. Mejias, Chem. Phys. Lett. 314 (1999) 558–563.
[15] D. Simpson, Surf. Sci. 516 (2002) 134–146.
[16] A. Fedorockova, P. Raschman, Chem. Eng. J. 143 (2008) 265–272.
[17] D. Ferry, Surf. Sci. 409 (1998) 101–116.
[18] P. Liu, Surf. Sci. 412–413 (1998) 287–314.
[19] Y. Yu, Q. Guo, S. Liu, E. Wang, P. Møller, Phys. Rev. B 68 (2003) 115414.
[20] Y.D. Kim, J. Stultz, D.W. Goodman, J. Phys. Chem. B 106 (2002) 1515–1517.
[21] H. Shin, J. Jung, K. Motobayashi, S. Yanagisawa, Y. Morikawa, Y. Kim, M. Kawai, Nat. Mater. 9 (2010) 442–447.
[22] M.A. Johnson, E.V. Stefanovich, T.N. Truong, J. Günster, D.W. Goodman, J. Phys. Chem. B 103 (1999) 3391–3398.
[23] L. Giordano, J. Goniakowski, J. Suzanne, Phys. Rev. Lett. 81 (1998) 1271–1273.
[24] F. Tielens, C. Minot, Surf. Sci. 600 (2006) 357–365.
[25] D. Costa, C. Chizallet, B. Ealet, J. Goniakowski, F. Finocchi, J. Chem. Phys. 125 (2006) 054702.
[26] I. Gay, N. Harrison, Surf. Sci. 591 (2005) 13–22.
[27] C.A. Scamehorn, N.M. Harrison, M.I. McCarthy, J. Chem. Phys. 101 (1994) 1547.
[28] J. Ahdjoudj, A. Markovits, C. Minot, Catal. Today 50 (1999) 541–551.
[29] N.H. de Leeuw, G.W. Watson, S.C. Parker, J. Phys. Chem. 99 (1995) 17219–17225.
[30] A.L. Almeida, J.B.L. Martins, C.A. Taft, E. Longo, W.A. Lester, J. Chem. Phys. 109 (1998) 3671.
[31] Y. Wang, T.N. Truong, J. Phys. Chem. B 108 (2004) 3289–3294.
[32] C. Chizallet, G. Costentin, M. Che, F. Delbecq, P. Sautet, J. Phys. Chem. B 110 (2006) 15878–15886.
[33] J. Cho, J. Park, K. Kim, Phys. Rev. B 62 (2000) 9981–9984.
[34] M. Odelius, Phys. Rev. Lett. 82 (1999) 3919–3922.
[35] W. Halim, Appl. Surf. Sci. 221 (2004) 53–61.
[36] G. Song, Adv. Eng. Mater. 7 (2005) 563–586.
[37] G.L. Song, A. Atrens, Adv. Eng. Mater. 1 (1999) 11–33.
[38] Y. Kojima, T. Aizawa, S. Kamado, K. Higashi, Mater. Sci. Forum 419–422 (2003) 3–20.
[39] G. Benhamu, D. Eliezer, K. Shin, S. Cohen, J. Alloys Compd. 431 (2007) 269–276.
[40] J. Chang, X. Guo, S. He, P. Fu, L. Peng, W. Ding, Corros. Sci. 50 (2008) 166–177.
[41] J. Zhang, X. Niu, X. Qiu, K. Liu, C. Nan, D. Tang, J. Meng, J. Alloys Compd. 471 (2009) 322–330.
[42] J.W. Chang, L.M. Peng, X.W. Guo, A. Atrens, P.H. Fu, W.J. Ding, X.S. Wang, J. Appl. Electrochem. 38 (2007) 207–214.
[43] M. Liu, P. Schmutz, P.J. Uggowitzer, G. Song, A. Atrens, Corros. Sci. 52 (2010) 3687–3701.
[44] P.L. Miller, B.A. Shaw, R.G. Wendt, W.C. Moshier, Corrosion 51 (1995) 922.
[45] S. Krishnamurthy, M. Khobaib, E. Robertson, F. Froes, Mater. Sci. Eng. 99 (1988) 507–511.
[46] H. Yao, Electrochim. Acta 48 (2003) 4197–4204.
[47] J. Zhang, D. Zhang, Z. Tian, J. Wang, K. Liu, H. Lu, D. Tang, J. Meng, Mater. Sci. Eng. A 489 (2008) 113–119.
[48] F. Rosalbino, E. Angelini, S. Denegri, A. Saccone, S. Delfino, Intermetallics 14 (2006) 1487–1492.
[49] Y. Song, Y. Liu, S. Wang, S. Yu, X. Zhu, Mater. Corros. 58 (2007) 189–192.
[50] M. Montemor, A. Simoes, M. Carmezim, Appl. Surf. Sci. 253 (2007) 6922–6931.
[51] H. Ardelean, I. Frateur, P. Marcus, Corros. Sci. 50 (2008) 1900–1906.
[52] G. Kresse, Comput. Mater. Sci. 6 (1996) 15–50.
[53] G. Kresse, Phys. Rev. B 59 (1999) 1758–1775.
[54] J.P. Perdew, K. Burke, M. Ernzerhof, Phys. Rev. Lett. 77 (1996) 3865–3868.
[55] K. Momma, F. Izumi, J. Appl. Crystallogr. 41 (2008) 653–658.
[56] B. Billings, American Institute of Physics. American Institute of Physics Handbook, 3rd ed., McGraw-Hill, New York, 1972.
[57] P. Haas, F. Tran, P. Blaha, Phys. Rev. B 79 (2009) 085104.
[58] D.O. Scanlon, A. Walsh, B.J. Morgan, M. Nolan, J. Fearon, G.W. Watson, J. Phys. Chem. C 111 (2007) 7971.
[59] H. Freund, G. Pacchioni, Chem. Soc. Rev. 37 (2008) 2224.
[60] I. Yudanov, G. Pacchioni, K. Neyman, N. Rösch, J. Phys. Chem. B 101 (1997) 2786–2792.
[61] A. Markovits, J. Paniagua, N. López, C. Minot, F. Illas, Phys. Rev. B 67 (2003).
[62] Y. Wang, E. Florez, F. Mondragon, T. Truong, Surf. Sci. 600 (2006) 1703–1713.
[63] G. Henkelman, B.P. Uberuaga, H. Jonsson, J. Chem. Phys. 113 (2000) 9901.
[64] R. Bader, Atoms in Molecules: A Quantum Theory, Clarendon Press/Oxford University Press, Oxford [England]/New York, 1994.
[65] G. Madsen, C. Gatti, B. Iversen, L. Damjanovic, G. Stucky, V. Srdanov, Phys. Rev. B 59 (1999) 12359–12369.
[66] K.B. Wiberg, P.R. Rablen, J. Comput. Chem. 14 (1993) 1504–1518.
[67] F. De Proft, C. Van Alsenoy, A. Peeters, W. Langenaeker, P. Geerlings, J. Comput. Chem. 23 (2002) 1198–1209.
[68] W. Tang, E. Sanville, G. Henkelman, J. Phys.: Condens. Matter 21 (2009) 084204.